Postprint *International Journal of Heat and Fluid Flow*, Vol.**43**, pp.15-25 (2013)
DOI: 10.1016/j.ijheatfluidflow.2013.05.013

Effect of Temperature Gradient within a Solid Particle on the Rotation and Oscillation Modes in Solid-dispersed Two-Phase Flows

Shintaro Takeuchi[1], **Takaaki Tsutsumi**[1] **and Takeo Kajishima**[1]

[1] Department of Mechanical Engineering, Osaka University

2-1 Yamada-oka, Suita-city, Osaka 565-0871 Japan

Abstract

Liquid-solid two-phase flow with heat transfer is simulated, and the effect of temperature gradient within a solid particle on the particle behaviour and heat transfer is studied. The interaction between fluid and particles is considered with our original immersed solid approach on a rectangular grid system. The local heat flux at the fluid-solid interface is described with an anisotropic heat conductivity matrix, and the governing equation of temperature is time-updated with an implicit treatment for the diffusion term. The method is applied to a 2-D natural convection flow of a relatively low Rayleigh number including multiple particles. Heat transfer and particle behaviours are studied for different solid heat conductivities (ratio to the fluid conductivity ranging between 10^{-3} and 10^{3}) and solid volume fractions. Under a condition of relatively low heat conductivity ratio, the particles show a simple circulating flow. By increasing the heat conductivity ratio, a transition of the particulate flow is observed to oscillation mode around the domain centre due to the buoyancy force as a restitution force. The oscillation period is found to vary with the heat conductivity ratio, and it is related to the time scales for the heat transfer via fluid and solid.

keywords: Multiphase flow, Solid-dispersion, Immersed solid object, Thermal flow, Heat conductivity

1 Introduction

Multiphase flow involving heat transfer is observed in industrial applications and natural phenomenon. For numerical modelling of solid-dispersed two-phase flows, especially in large scale systems, particles are often treated as a homogeneous media or continuous and fully inter-penetrating two-fluid media. In such cases with a large number of particles, a unique temperature is assumed for each particle and a simplified/empirical heat exchange model is applied at the fluid-solid interface.

However, particles placed in a temperature gradient could have characteristic heat transfer mechanism. For examples in catalyst engineering, a catalyst particle could encounter a meltdown depending on its surrounding gas flow and its size (McKenna et al. 1995). Gan et al. (2003b) studied the effect of thermal convection on the sedimentation process of particles and Gan et al. (2003a) further reported the enhanced study on sedimentation with melting solid particles by a finite-element method with an arbitrary Lagrangian Eulerian technique for the moving internal boundaries. Also for studying the general effects on the local heat transfer mechanism at the object surface, heat transfer in steady and transient flows was studied with a body-fitted mesh (Moukalled and Darwish 1997; Feng and Michaelides 2000).

For specific applications, such as heat transfer in a system including a large number of particles moving relative to each other, a fixed-grid approach (e.g., immersed boundary method) may be more advantageous. There exist several numerical studies of heat transfer problem in (fully resolved) solid-dispersed multiphase flow on a uniformly distributed rectangular grid system by using immersed boundary technique. Most of those propose a procedure for enforcing iso-thermal and/or iso-heat-flux conditions at the fluid-solid interface based on the framework of fixed-grid methods, mainly on direct-forcing immersed boundary methods. Though iso-thermal condition is relatively straightforward to implement, the importance of the adiabatic condition of the passive scalar on the immersed boundary was first reported by Fadlun et al. (2000). When they visualised the simulation result of their direct forcing immersed boundary method with the passive scalar, the no-flux condition on the immersed boundary was hard to be accurately satisfied (Kim and Choi 2004). Kim et al. (2001) and Kim and Choi (2004) proposed an immersed boundary method for imposing iso-thermal and iso-heat-flux boundary conditions on the immersed boundary. A heat source/sink is given on the boundary or inside the body so as to attain a desired temperature condition determined by a bi-linear/linear interpolation from the adjacent cells. The heat source/sink method was applied to analyse the turbulent heat transfer in a dimpled channel (Lee et al. 2007) and heat transfer around a circular cylinder (Yoon et al. 2007; Kim et al. 2008).

A similar heat source/sink approach is proposed by Pacheco et al. (2005) and Pacheco-Vega et al. (2007) with a successive determination algorithm of the temperatures inside the body to match the iso-thermal and iso-heat-flux conditions at the immersed boundary. They generalised those boundary conditions into a set of

equations, which facilitates the application to a Robin boundary condition, and they showed that the method has a second-order accuracy with respect to the grid size. Pan (2006) solved forced and natural convection problems by an immersed boundary technique on Cartesian mesh by approximating the flow variables at the interface cells with a volume average of those of the mixture (solid and fluid).

Ren et al. (2012) proposed an implicit formulation of the momentum and heat source/sink approach. The boundary force and heat flux are solved implicitly (with the matrix of components of discretised pseudo delta function) so that the no-slip and fixed temperature conditions are enforced on the immersed boundary. Though the numerical procedure is split into several parts, the idea is close to a distributed Lagrangian multiplier method in the sense that the boundary-forcing and boundary-energy terms are determined to attain the desirable velocity and temperature at the boundary. As a new type of boundary treatment for heat and fluid flows, Jeong et al. (2010) proposed a combined IB-lattice Boltzmann approach that employs the equilibrium velocity and equilibrium internal energy density to couple the flow (on the Eulerian grid) and heat transfer (on the Lagrangian points).

While the above researchers simplify the problem by imposing a boundary condition of either constant temperature or constant flux (or combination of those), there also exist many situations where temperature gradient develops within the solid object and neither boundary condition is applicable. Iaccarino et al. (2002) solved heat and fluid flows in a 2-D ribbed channel with a more natural boundary condition at the object surface. Though the surfaces of the rectangular ribs were aligned to match the cell faces, the effect of temperature distribution within the object and heat exchange between the fluid and solid were considered. Later, Iaccarino and the co-workers (Mittal and Iaccarino 2005; Iaccarino and Moreau 2006) proposed a second-order interpolation scheme (linear in the tangential direction and quadratic in the normal direction) for immersed boundary problems. Kang et al. (2009) employed an immersed boundary method and proposed a method to consider temperature distribution within the particle by updating the boundary condition at the voxel (cuboid)-face for determining the interface temperature and heat flux.

Other examples of heat transfer problems involving the solid heat conduction (conjugate heat transfer problem) are the approaches using body-fitted unstructured mesh. McKenna et al. (1999) employed unstructured mesh and solved steady heat transfer problem for catalyst particle system in a stream employing some fixed (binary-distributed) particles under several spatial configurations, and concluded that, in the vicinity of a large particle, the effect of conduction is significant for a small particle compared with the contribution of the convection. Nijemeisland and Dixon (2004) simulated a heat transfer problem of gas flow through fixed layers of nearly-touching particles with unstructured mesh, and they studied characteristic flow patterns in the inter-particle regions influenced by the wall heat flux.

Despite the importance of moving particle on the conjugate heat transfer problems in multiphase flows, the numerical study so far largely focused on the heat transfer problems with fixed particles.

Zhang et al. (2008) studied a heat transfer problem past an externally-oscillating cylinder on a rectangular grid system by using a heat source/sink approach based on the direct-forcing immersed boundary. To give a constant heat-flux condition at the object surface, they set out a layer of virtual points outside the physical immersed boundary (Lagrangian markers). The temperatures on the Lagrangian markers are determined such that the desired normal derivative of temperature at the surface is satisfied with the temperature of the virtual points interpolated from the surrounding Eulerian grid points. They mentioned that their method avoids an unphysical heat accumulation inside the particle caused by source/sink methods. Heat transfer between fluid and freely-moving particles was simulated by Yu et al. (2006) by their fictitious domain method. They attempted to evaluate the contributions of the convection and conduction by particles. Though this is a two-dimensional study, this is one of the pioneering studies for dealing with the heat transfer in solid-dispersed multiphase flows.

One of the present authors proposed a new method (Ueyama et al. 2011) for solving a heat-transfer problem in a solid-liquid two-phase flow on a fixed grid. In the present work, a new heat conduction model is proposed for the heat conduction at the solid-fluid interface. We show some simulation results of heat transfer problem in a multiphase flow of dispersed solid particles considering the temperature gradient within the solid object (and therefore local heat flux at the surface). In order to employ a large number of particles moving relatively to each other, we solve the temperature field in an Eulerian coordinate system, and this method avoids the temperature-matching process (at the particle surface) obtained in the interior and exterior of the solid object. The heat conduction model is thoroughly validated through comparison with the analytical solution of a heat conduction problem involving a tangential temperature gradient along the fluid-solid interface.

The interaction between fluid and particles is solved with our original immersed solid approach (Kajishima et al. 2001; Yuki et al. 2007) on a rectangular grid system. The method employs a simple procedure for the momentum-exchange by imposing a volume force (as interaction force) on both solid and fluid phases. The method has been applied for studying a clustering process with 1000 spherical particles in a turbulent flow (Kajishima et al. 2001; Kajishima and Takiguchi 2002; Kajishima 2004). Also the method was applied to the analysis of sedimentation process employing a total of 10^5 spherical particles by Nishiura et al. (2006).

In the present study, we applied the method to a 2-D solid-dispersed two-phase flow in a confined square domain under a relatively low Rayleigh number condition. Heat transfer and characteristic particle behaviours are studied for different ratios of heat conductivity (solid to liquid). Through consideration of

the highlighted effects of temperature distributions within the particles and liquid, the effect of heat transfer through solid material on the interaction between fluid and solid is studied.

2 Governing Equations and Numerical Methods

2.1 Governing equations

Fluid is assumed to be incompressible and Boussinesq approximation is employed to include the effect of density fluctuation. Viscous dissipation of kinetic energy is assumed to have negligible contribution to the increase in internal energy.

The equations of continuity, momentum and energy are as follows:

$$\begin{aligned}
&\nabla \cdot \boldsymbol{u}_f = 0 \,, \\
&\rho_f \frac{\partial \boldsymbol{u}_f}{\partial t} + \rho_f \boldsymbol{u}_f \cdot \nabla \boldsymbol{u}_f = -\nabla p + \nabla \cdot \left(\mu_f \left(\nabla \boldsymbol{u}_f + (\nabla \boldsymbol{u}_f)^T \right) \right) + \rho_f \beta (T - T_0) \boldsymbol{g} \,, \\
&\frac{\partial \rho_f c_f T}{\partial t} + \boldsymbol{u}_f \cdot \nabla (\rho_f c_f T) = \nabla \cdot (\lambda_f \nabla T) \,,
\end{aligned} \tag{1}$$

where $\boldsymbol{u}_f$ is the fluid velocity, ρ_f the reference density, $\boldsymbol{g}$ the gravitational acceleration, β the coefficient of thermal expansion, T the temperature, T_0 the reference temperature, c_f the specific heat. In the following, viscous coefficient (μ_f), heat capacity ($\rho_f c_f$) and heat conductivity (λ_f) are assumed to be constant.

Governing equations for the motion of the solid object is Newton's equations of momentum and angular momentum:

$$m_p \frac{d\boldsymbol{v}_p}{dt} = \boldsymbol{F} + \boldsymbol{G}_p \,, \qquad \boldsymbol{I}_p \frac{d\boldsymbol{\omega}_p}{dt} = \boldsymbol{T} + \boldsymbol{N}_p$$

where m_p is the mass, $\boldsymbol{I}_p$ the inertia tensor, $\boldsymbol{v}_p$ the translating velocity, $\boldsymbol{\omega}_p$ the angular velocity, $\boldsymbol{F}$ and $\boldsymbol{T}$ the hydrodynamic force and its moment, respectively, and $\boldsymbol{G}_p$ and $\boldsymbol{N}_p$ are external force and torque, respectively.

2.2 Fluid-solid interaction model: immersed solid approach

Momentum exchange at the fluid-solid interface, where a cell is partially occupied by a solid particle, is solved by the immersed solid approach developed by Kajishima and the co-workers (Kajishima et al. 2001; Kajishima and Takiguchi 2002), on a uniformly distributed fixed mesh system. The basic idea is briefly described below.

First, the whole field is treated as a single continuum and time-updated together with the continuity equation. Because this velocity field does not satisfy the no-slip condition at the solid surface, an interaction term is included. Here, the interaction term is modelled to be proportional to the local solid volume fraction

α ($0 \leq \alpha \leq 1$) and the relative velocity of the local solid to the fluid, and we treat the interaction term to distribute fluid-solid interface region as well as within the solid object, like a body force. The object experiences the same force in the opposite direction. Therefore, the surface integration of hydrodynamic force is replaced with the volume integration of the interaction term (with the negative sign) over the region enclosing the object. This replacement from surface to volume integrations considerably facilitates the computation of the solid motion, and also the use of the same body force for both (fluid and particle) phases in a shared Cartesian cell ensures momentum conservation between the phases. More details of the above immersed solid approach are found in the literatures listed in the reference (Kajishima et al. 2001; Yuki et al. 2007).

Translating and angular velocities are time-updated by a predictor-corrector method (Ueyama et al. 2011), which was shown to be applicable to solid-liquid interaction problems involving a range of density ratio. Then, the new position of the particle is obtained, and the local solid volume fraction α and surface normal vector with respect to the new position are determined accordingly.

2.3 Temperature field and interfacial heat conduction model

Temperature field for the mixture of the fluid and solid is treated in an Eulerian way. Cell temperature is established as the volume-averaged local thermal energy divided by the heat capacity of the mixture. This coincides with the locally-averaged temperature field at the first order accuracy with respect to the local solid volume fraction. For more detail, see Appendix A. In the present study, to see the isolated effect of heat conductivities on the heat transfer from solid to fluid (and vice versa), all the numerical simulations are conducted under $\rho_s = \rho_f (= \rho)$ and $c_s = c_f (= c)$, which guarantees the coincidence of the above two temperatures.

The temperature equation for the mixture

$$\frac{\partial \rho c T}{\partial t} + \boldsymbol{u} \cdot \nabla(\rho c T) = \nabla \cdot (\lambda \nabla T) \tag{2}$$

is time-updated by the Crank-Nicolson method for the diffusion term. Here, $\lambda(\boldsymbol{x})$ is the distributed heat conductivity.

In an interfacial cell partially occupied by a solid object, the discretised temperature gradient ($\nabla T|_{ij}$) is decomposed into surface-normal and tangential components, and those components are multiplied by the following mean heat conductivities:

$$\frac{1}{\lambda_h} = \frac{1-\alpha}{\lambda_f} + \frac{\alpha}{\lambda_p}\,, \qquad \lambda_a = (1-\alpha)\lambda_f + \alpha\lambda_p\,, \tag{3}$$

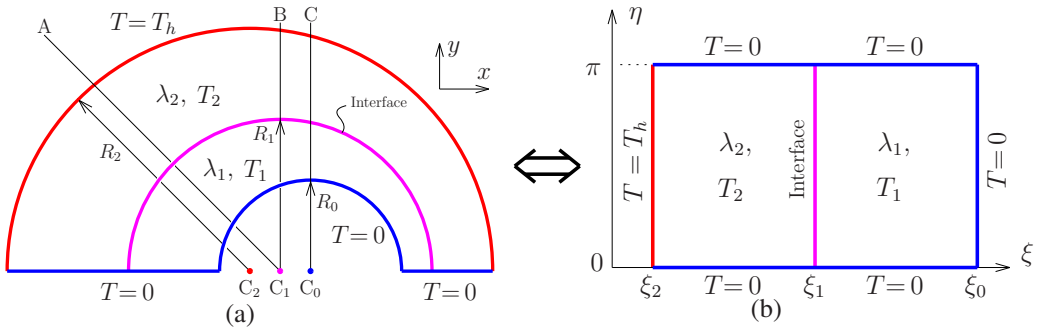

Figure 1: Schematic of a heat conduction problem through eccentric cylinders: (a) physical plane and (b) converted plane. Cross-sections A, B and C are inclined $135°$, $90°$ and $90°$ against x-axis and go through C_2, C_1 and C_0, respectively.

where α is the local solid volume fraction. Assuming that both fluid and solid has the same interfacial temperature, the heat flux $\boldsymbol{q}_\mathrm{I}$ in the interfacial cell (cell indices i and j) is given by the following equation:

$$-\boldsymbol{q}_\mathrm{I}|_{ij} \quad = \quad [\lambda_a \boldsymbol{I} + (\lambda_h - \lambda_a)(\boldsymbol{nn})]_{ij} \cdot \nabla T|_{ij} \ , \tag{4}$$

where $\boldsymbol{I}$ is the identity matrix and $\boldsymbol{n}$ is the unit outward normal vector at the object surface. The above formula includes both tangential and normal fluxes in one equation, which accounts for the temperature gradients in both fluid and solid phases represented by the cell averaged temperature. For more detail, see Appendix B. Note that this treatment of heat flux at the surface shows good compatibility with our immersed solid approach; since α distributes in an interfacial cell in our model, we need no extra discretisation efforts for calculating $\boldsymbol{q}_\mathrm{I}$ in the interfacial cell, but the heat flux is simply constructed by Eq.(4) with α and $\boldsymbol{n}$ as if anisotropic heat conductivity distributes in the interfacial cell.

In the following sections, the above heat flux is applied to a circular geometry. However, the formula is not restricted to circular/spherical geometry; our fluid-solid interaction approach is also applicable to solid objects of arbitrary shape (Yuki et al. 2007; Takeuchi et al. 2009).

3 Validation

The validity of the heat flux model is assessed here. A problem of heat conduction through a pair of eccentric cylinders with different heat conductivities is arranged. As illustrated in Fig. 1(a), the problem highlights both normal and tangential components of the temperature gradient along the interface (an arc of radius R_1).

Let us consider the following conformal mapping $(x, y) \to (\xi, \eta)$

$$\xi = \frac{1}{2} \log \frac{(x-1)^2 + y^2}{(x+1)^2 + y^2}, \quad \eta = \arctan \frac{2y}{x^2 + y^2 - 1} \ . \tag{5}$$

DOI: 10.1016/j.ijheatfluidflow.2013.05.013

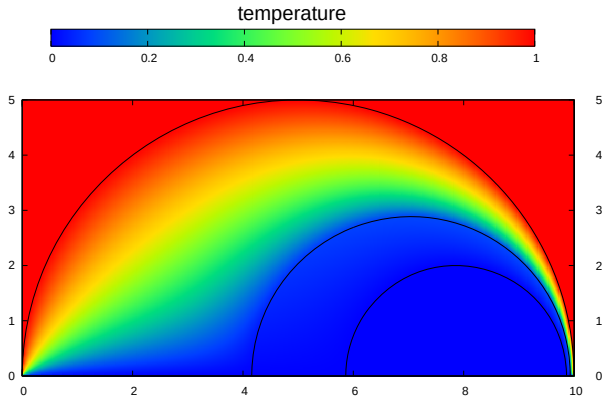

Figure 2: Temperature distribution within two eccentric cylinders. The following conditions are set: $R_0 = 2, R_2 = 5, \lambda_1/\lambda_2 = 10, T_h = 1$.

Curves $\xi = \xi_c$ (ξ_c: constant) are mapped to the following eccentric circles having the centres on x-axis:

$$(x + \coth \xi_c)^2 + y^2 = \mathrm{cosech}^2 \xi_c \ . \tag{6}$$

Given two boundary radii (R_0 for inner and R_2 for outer boundaries, respectively) on x-y plane, the corresponding straight lines $\xi = \xi_0$ and $\xi = \xi_2$ are set to the two boundaries on ξ-η plane. From Eq.(6), the values ξ_0 and ξ_2 are obtained as $\xi_i = \sinh^{-1}(1/R_i)$ $(i = 0, 2)$. For the convenience, we set the radius of the interface as $R_1 = 1/\sinh \xi_1$ where $\xi_1 = (\xi_0 + \xi_2)/2$.

The heat conductivities in the inner and outer regions (region 1 and 2, respectively), are set to λ_1 and λ_2, respectively. With the boundary temperatures $T = T_h$ on the C_2-circumference (i.e., $\xi = \xi_2$) and $T = 0$ otherwise ($\xi = \xi_0$ and $\eta = 0, \pi$), the temperatures in region 1 and 2 are determined as follows:

$$T_1 = \frac{2}{\pi} \sum_{n=1,3,5,\cdots}^{\infty} \frac{2}{n} \frac{T_\lambda}{\sinh(n\Delta\xi_{01}) \cosh(n\Delta\xi_{01})} \sinh(n(\xi_0 - \xi)) \sin n\eta \tag{7a}$$

$$\begin{aligned} T_2 = {} & \frac{2}{\pi} \sum_{n=1,3,5,\cdots}^{\infty} \frac{2}{n} \frac{T_\lambda}{\sinh(n\Delta\xi_{12}) \cosh(n\Delta\xi_{12})} \sinh(n(\xi - \xi_2)) \sin n\eta \\ & + \frac{2}{\pi} \sum_{n=1,3,5,\cdots}^{\infty} \frac{2}{n} T_h \left[1 - \frac{\tanh(n(\xi - \xi_2))}{\tanh(n\Delta\xi_{12})} \right] \cosh(n(\xi - \xi_2)) \sin n\eta \end{aligned} \tag{7b}$$

$$\text{where} \quad T_\lambda = \frac{\lambda_2}{\lambda_1 + \lambda_2} T_h \ , \quad \Delta\xi_{ab} = \xi_a - \xi_b \ .$$

The derivation is detailed in Appendix C. The temperature distribution on x-y plane is given by substituting Eq.(5) into the above equations. Figure 2 shows a temperature distribution for a given set of dimensions and under the following parameters: $T_h = 1, \lambda_1 = 10\lambda_2$.

To assess the validity, steady temperature distribution is obtained by numerically solving $\nabla \cdot (\lambda \nabla T) = 0$ on a uniform rectangular grid system by varying the number of grid points in x and y directions in the

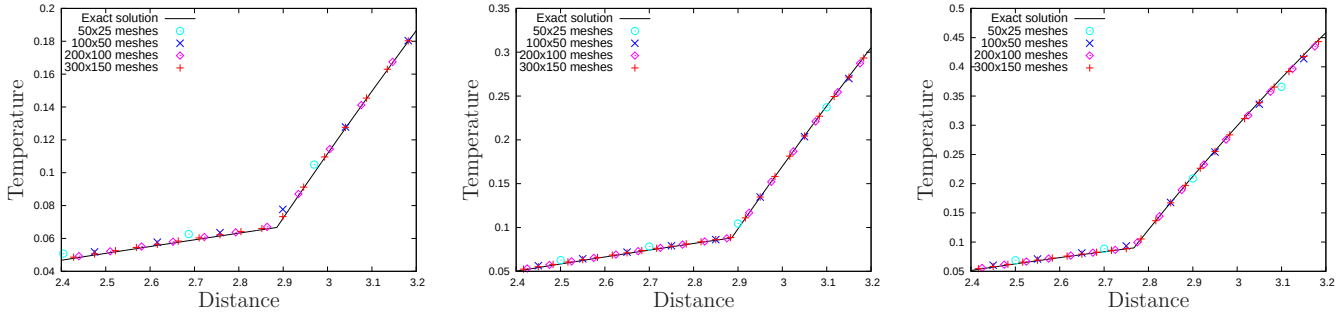

(a) Cross-section A (b) Cross-section B (c) Cross-section C

Figure 3: Cross-sectional temperature profiles in three directions (A, B and C) shown in Fig. 1(a). Plotted as a function of the distance from the corresponding circle centre.

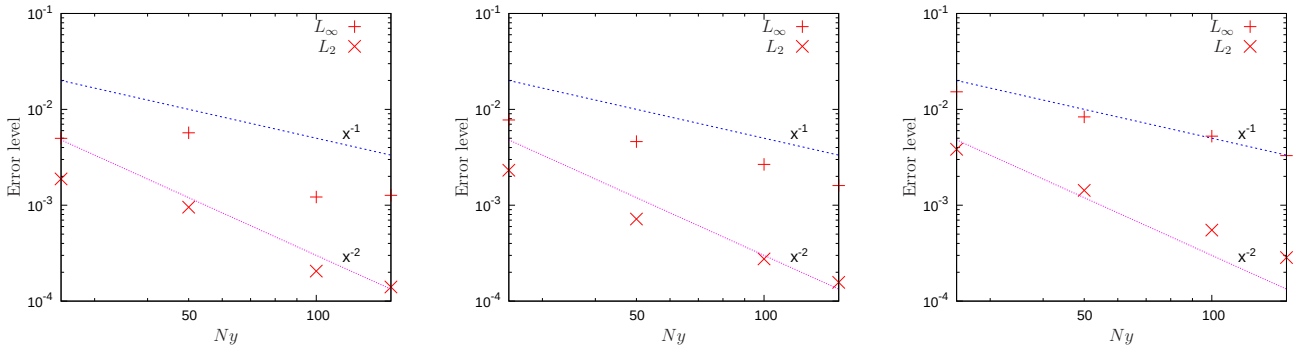

(a) Cross-section A (b) Cross-section B (c) Cross-section C

Figure 4: Grid convergence of the numerical solution plotted against the number of grid points in y direction.

following range: 50×25, 100×50, 200×100, 300×150. Here, Eq.(4) is used to calculate the flux at the interface.

The temperature distributions in three cross-sections, as illustrated in Fig. 1(a), are compared. Cross-sections A and B are, respectively, in $135°$ and $90°$ directions with respect to x-axis from C_2 and C_1, and cross-section C is in $90°$ direction from C_0. The interface point in the cross-section C will have the largest tangential component of the interfacial temperature gradient.

Figure 3 compares the numerical and analytical profiles of the temperature. The numerical results show good agreement with the analytical solution. The error is evaluated with L_2 and L_∞ norms, and plotted in Fig. 4 as a function of the number of grid points in y direction. In all the cross-sections, the numerical solution converges to the analytical one monotonously as the spatial resolution increases. The error in cross-section C is found to converge at the rate of $\Delta^{-1.42}$ by L_2-norm, where Δ is grid spacing.

The above result shows that the flux decomposition at the interface, Eq.(4), is applicable to the Cartesian mesh and guarantees the validity of the interfacial flux model.

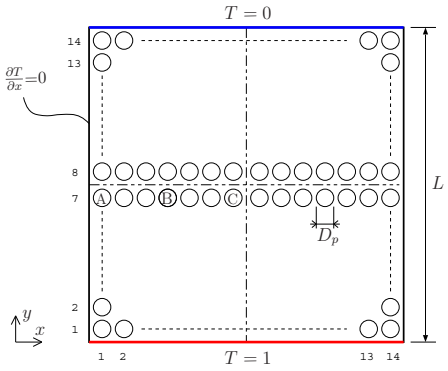

Figure 5: Schematic of the arrangement of the particles in a square domain. A total of 196 ($= 14 \times 14$) particles are employed. The particles labelled with "A", "B" and "C" are, respectively, located on the first, fourth and seventh column from the left wall on the seventh raw from the bottom.

Table 1: Simulation parameters

Num. of grid points	$N_x \times N_y$	200×200
Number of particles	N_p	14^2
Diameter of particles	D_p	$0.05L$
Rayleigh number	Ra	1×10^4
Heat conductivity ratio	λ_s/λ_f	$10^{-3}, 10^0, 10^1, 10^2, 10^3$

4 Results and Discussion

Particle behaviour in natural convection in a closed domain is studied. In the present work, the computational domain is a square shape of side length L, and the particles are initially arranged uniformly in the domain as illustrated in Fig.5. Temperature difference between the top and bottom walls is kept constant ($\Delta T = 1$), and no heat flux is given at the lateral walls. The no-slip boundary condition and the Neumann condition are applied to the velocity and pressure, respectively, on the solid walls. The equations are non-dimensionalised with reference length L, reference velocity $U = \sqrt{g\beta\Delta T L}$, reference pressure $\rho_f U^2$ and characteristic temperature difference ΔT. The non-dimensional numbers used here are Rayleigh number (Ra) and Prandtl number (Pr). To investigate the effect of natural convection on the particle behaviour and heat transfer, Prandtl number, density ratio and specific heat ratio are set to unity. In the following, unless specified otherwise, time increment is set depending on the heat conductivity ratio (of solid to fluid); $\Delta t = 10^{-3}$ for $\lambda_s/\lambda_f \leq 10^2$ and $\Delta t = 5 \times 10^{-4}$ for $\lambda_s/\lambda_f > 10^2$.

For particle-particle interaction, a discrete element model with soft-sphere collision (Tsuji et al. 1993) is applied.

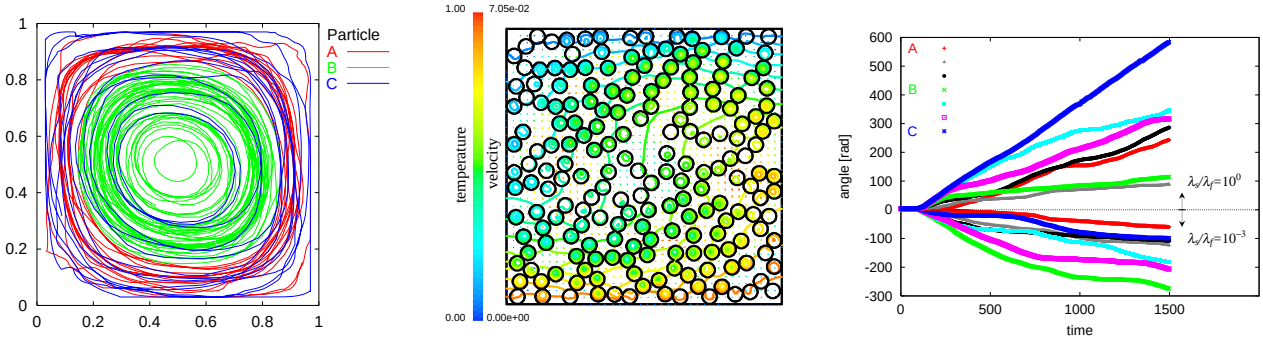

(a) (b) (c)

Figure 6: Motion of the particles of a low ratio of heat conductivities ($\lambda_s/\lambda_f = 10^{-3}$). (a) Trajectories of the labelled particles (see Fig. 5) in the time range $500 \leq t \leq 1500$. (b) Instantaneous particle positions with the velocity and temperature fields at $t = 1500$. (c) Time history of the angular positions of the labelled particles and the horizontal neighbours. The angle is measured in the counter-clockwise direction around the domain centre from the positive x-axis.

Effect of heat conductivities

Fluid and particles motions are simulated for different ratios of heat conductivity (solid to fluid), and we look into the effect of temperature distribution within the particle on the coherent motions of the particles. The parameters and conditions are summarized in Table 1. The particle Reynolds number (based on D_p and the natural convection speed driven by the vertical temperature difference across D_p) corresponding to the Ra is 25 at most for a fixed particle. The solid volume fraction is 38.5%.

For particles of $\lambda_s/\lambda_f = 10^{-3}$ and 10^0, the fluid and particles are found to go around in one direction around the domain centre, like a Rayleigh-Bénard convection at low Rayleigh numbers. The trajectories of the labelled particles (see Fig.5) are shown in Fig.6(a) for the case of $\lambda_s/\lambda_f = 10^{-3}$. Though particles "A" and "B" rather stay in the outer and inner regions of the domain, respectively, particle "C" moves from deep inside the domain to the wall region back and forth. Eventually, mixing of the particles is enhanced as shown in the snapshot of Fig.6(b). Figure 6(c) shows the time histories of angular positions (together with some neighbouring particles) for the cases of the two heat conductivity ratios. The angle is measured in the counter-clockwise direction around the domain centre from the positive x-axis. From the figure, all the particles rotate at the respective angular speeds in single directions. No further change in rotating state (for each case) is observed within the time range investigated ($t \leq 1500$).

On the other hand, in the range of conductivity ratio $\lambda_s/\lambda_f \geq 10^1$, characteristic oscillatory mode of particles is observed around the domain centre. Figure 7 shows the typical two time-developments of the angular positions of the particle "B"; the case of $\lambda_s/\lambda_f = 10^2$ exhibits a constant oscillation period until

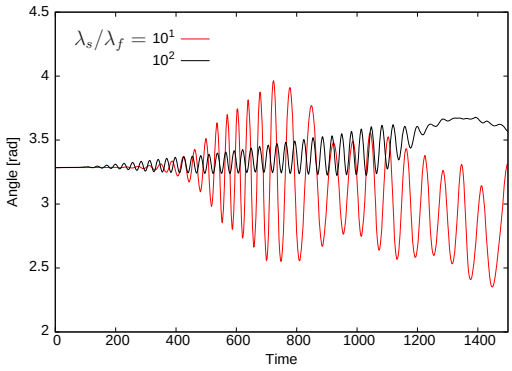

Figure 7: Typical time developments of the angular positions of particle "B". The angle is measured in the counter-clockwise direction around the domain centre from the positive x-axis.

t=1100, whereas the oscillation frequency for the case of $\lambda_s/\lambda_f = 10^1$ alters around $t = 700$ when the exponential increase of the amplitude reaches the local maximum. Snapshots of the particles and temperature contours for $\lambda_s/\lambda_f = 10^1$ are shown in Fig.8. Figure 8(a) is a moment when the particles are in a resting state after travelling in the clockwise direction. Then, the particles turn in the opposite direction and, half period later, the particles are displaced most as Fig.8(b) shows and soon starts rotating in the clockwise direction, again. Surprisingly, the array of the particles are kept (relatively) ordered even after (perceivable) ten oscillation periods, which is in contrast with the mingled state of the particles in Fig.6(b). The oscillating behaviour is also observed in cases with a slightly lower bulk solid volume fraction in a range between 25 and 32% (with keeping the same initial particle arrangement and $\lambda_s/\lambda_f = 10^2$), however, in the case of bulk solid volume fraction 25%, it changes to a rotating mode after several periods of the oscillation. This preliminary parametric study suggests that the oscillation of the particle system would be observed in a relatively wide range of bulk concentration, given an appropriate initial inter-particle distance such that the convection does not develop too much within the characteristic time of the heat conduction through the solid.

The restitution of the particle motion may be explained as follows. Two particles located on the other side with respect to the domain centre will experience different hydrodynamic forces depending on the distance from the bottom hot wall, giving rise to an imbalance of the angular momentum. Assuming that the temperature field responds immediately to the displacement of the particles, the angular position θ of the particle will be governed by an equation of the form $\ddot{\theta} = -\sin 2\theta$, and the period of the oscillation is given by a complete elliptic integral of the first kind. However, in reality, there is a finite time lag for the temperature field to respond to the motion of the particle. In Fig.8, when the particles are displaced most in the upper/lower side, the iso-contours of the temperature are aligned roughly horizontally. However, when the particles start moving in the opposite directions, the iso-thermal lines cross the solid particles quickly,

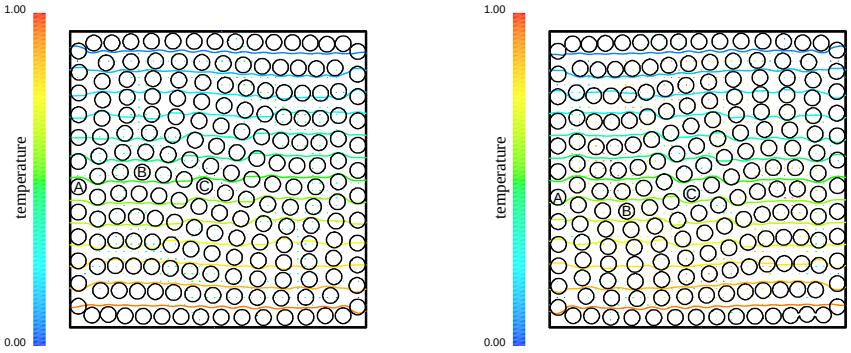

(a) $t = 516$ (b) half-period later ($t = 534$)

Figure 8: Instantaneous particle arrangements for the case of $\lambda_s/\lambda_f = 10^1$. A moment when the particles are in a resting state after travelling (a) in the clockwise direction and (b) in the counter-clockwise direction (half period later).

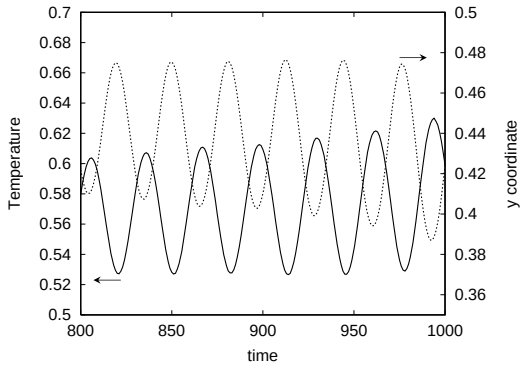

Figure 9: Time development of the temperature at the centre of oscillating particle "B" and y coordinate of the particle centre. The ratio of heat conductivity is $\lambda_s/\lambda_f = 10^2$.

causing local distortion of the iso-thermal lines. Figure 9 shows the time variation of the temperature at the centre of the particle "B" for $\lambda_s/\lambda_f = 10^2$ together with its y position. The particle temperature shows a small time lag with respect to the vertical motion.

As observed in Fig. 7, the amplitudes exhibit exponential increase in the initial development stage of the oscillation. The time-development of the angular position of the particle would be described as

$$A(r)\exp\left[(\chi_r + i\chi_i)t\right], \tag{8}$$

where i is the imaginary unit, r the radial position from the domain centre, and A, χ_r, χ_i are real numbers. This model also describes the rotating motion shown in Fig.6, and Table 2 summaries the sign of the eigen-frequencies of the angular motions of the particles in the studied range of the conductivity ratios.

Due to the positive values for χ_r and time-varying χ_i, this time-development model is only applicable to a limited time range of the initial development. Figure 10 plots the oscillation periods $\tau_R(= 2\pi/\chi_i)$ for

Table 2: Summary of the signs of the eigen frequencies (for different λ_s/λ_f) and the corresponding motion of the particles.

λ_s/λ_f	$10^{-3} \sim 10^{0}$	$10^{1} \sim 10^{3}$
χ_r	$+$	$+$
χ_i	0	$+$
	Rotation	Oscillation

different values of the heat conductivity ratio. With the minimum oscillation period at around $\lambda_s/\lambda_f = 10^2$, τ_R increases in both lower and higher sides with decreasing and increasing λ_s/λ_f, respectively. Also from the figure, strong correlations are found in the respective ranges of the heat conductivity ratio.

For particles of a sufficiently high conductivity ratio, assuming that a temperature field within the solid develops in the thermal diffusion time scale of the solid ($\tau_{sD} = (\rho c)_s D_p^2/\lambda_s$), the difference in the moment of the buoyancy on the two particles at θ and $(\theta + \pi)$ is roughly estimated by a one-dimensional heat conduction model as

$$\left(-\frac{2}{D_p} \frac{(\rho c)_f}{(\rho c)_s} \frac{\Delta T}{L} l \sin\theta \sqrt{4 a_f \tau_{sD}} + \text{Const.} \right) \rho g \beta V l \cos\theta$$

where l is the distance between the particle and the domain centre and $a_f = \lambda_f/(\rho c)_f$. Then a linear approximation for the equation of angular momentum gives a dependency of the oscillation period τ_R on the conductivity ratio as

$$\tau_R \propto \left(\frac{\lambda_s}{\lambda_f} \right)^{\frac{1}{4}} . \tag{9}$$

Figure 10 also plots the line of $1/4$ power of (λ_s/λ_f), and the graph shows a reasonable agreement with the above correlation.

The above τ_R is partly related to the time scales of heat transfer via the different materials, as follows. The characteristic fluid velocity is taken to the velocity induced by the vertical temperature difference across the particle diameter; $U_p = \sqrt{g\beta \left(\frac{\Delta T}{L} D_p\right) D_p}$. Then, the time scale of the convective heat transfer is $\tau_{fC} = D_p/U_p$, and its ratio to τ_{sD} is given as follows:

$$\frac{\tau_{fC}}{\tau_{sD}} = \left(\frac{\lambda}{\rho c} \right)_s \frac{1}{\nu_f} \frac{\nu_f}{D_p U_p} = \frac{\lambda_s}{\lambda_f} \frac{(\rho c)_f}{(\rho c)_s} \frac{1}{\mathrm{Pr}\sqrt{\mathrm{Gr}_p}} = \frac{\lambda_s}{\lambda_f} \frac{(\rho c)_f}{(\rho c)_s} \frac{\sqrt{\mathrm{Gr}_p}}{\mathrm{Ra}_p} ,$$

where the Grashof number Gr_p and the Rayleigh number Ra_p are based on D_p and U_p. The upper axis of Fig.10 also shows the time scale ratio τ_{fC}/τ_{sD} for comparison. The particle oscillation occurs when the thermal relaxation time scale in solid is one order of magnitude larger than that of the fluid convection in the present situation of the fixed ratio of the heat capacities of the materials. The above characteristic time scale is one of the key parameters for heat exchange and interaction between fluid and particles, and the

International Journal of Heat and Fluid Flow, Vol.**43**, pp.15-25 (2013)
DOI: 10.1016/j.ijheatfluidflow.2013.05.013

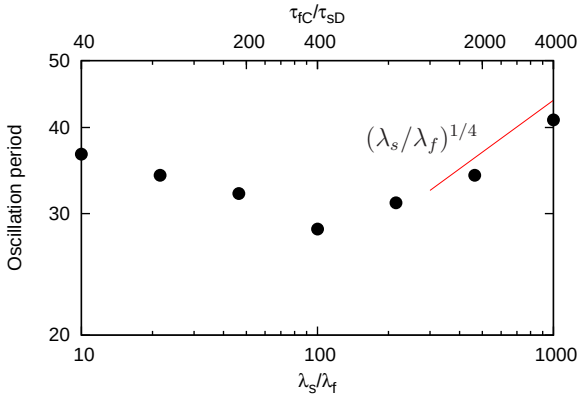

Figure 10: Dominant oscillation period against λ_s/λ_f. Non-dimensional characteristic time scale τ_{fC}/τ_{sD} is also shown on the top axis for comparison.

drastic change in particle motion (rotation or oscillation) suggests interesting implications for the change of the major heat transfer path in the particulate flow, depending on the heat conductivity ratio of solid to fluid.

5 Conclusions

Heat transfer problem in a solid-dispersed two-phase flow was simulated under relatively dense solid concentrations and a low Rayleigh number. The numerical method is based on our original immersed solid approach, and the local heat flux at the fluid-solid surface is treated by a new flux decomposition technique. The method was applied to a solid-dispersed 2-D confined flow with a constant temperature difference at the top and bottom walls, and the behaviour of the particles was studied for different heat conductivity ratios of solid to fluid. With particles of a low heat conductivity ratio, the particles show a circulating flow around the domain centre. By increasing the heat conductivity ratio, the particles were found to oscillate around the domain centre at a frequency determined by the thermal diffusion time scales. The oscillation period varies with the heat conductivity ratio, and the period was found to correlate with one quarter power of the conductivity ratio in a sufficiently high range of the conductivity ratio. Also, a correlation is suggested between the particle motion (rotation/oscillation) and the respective characteristic time scales of heat transfer via solid and fluid. The simulation results highlight the effect of temperature distributions within the particles, and, even for the ordered behaviour of the particles, the difference in time scales of heat transfer through the different materials plays an important role for the motion of the particulate flow.

References

Fadlun, E.A., Verzicco, R., Orlandi, P. and Mohd-Yusof, J., 2000, "Combined immersed-boundary finite-difference methods for three-dimensional complex flow simulations", *Journal of Computational Physics* **161**, pp.35-60

Feng, Z.-G. and Michaelides, E.E., 2000, "A numerical study on the transient heat transfer from a sphere at high Reynolds and Peclet numbers", *International Journal of Heat and Mass Transfer* **43**, pp.219-229

Gan, H., Feng, J.J. and Hu, H.H., 2003, "Simulation of the sedimentation of melting solid particles", *International Journal of Multiphase Flows* **29**, pp.751-769

Gan, H., Chang, J., Feng, J. and Hu, H.H., 2003, "Direct numerical simulation of the sedimentation of solid particles with thermal convection", *Journal of Fluid Mechanics* **481**, pp.385-411

Iaccarino, G. and Moreau, S., 2006, "Natural and forced conjugate heat transfer in complex geometries on cartesian adapted grids", *Transaction of the ASME* **128**, pp.838-846

Iaccarino, G., Ooi, A., Durbin, P.A. and Behnia, M., 2002, "Conjugate heat transfer predictions in two-dimensional ribbed passages", *International Journal of Heat and Fluid Flow* **23**, pp.340-345

Jeong, H.K., Yoon, H.S., Ha, M.Y. and Tsutahara, M., 2010, "An immersed boundary-thermal lattice Boltzmann method using an equilibrium internal energy density approach for the simulation of flows with heat transfer", *Journal of Computational Physics* **229**, pp.2526-2543

Kajishima, T., Takiguchi, S., Hamasaki, H. and Miyake, Y., 2001, "Turbulence structure of particle-laden flow in a vertical plane channel due to vortex shedding", *JSME International Journal Series B*, **44**-4, pp.526-535

Kajishima, T. and Takiguchi, S., 2002, "Interaction between particle clusters and fluid turbulence", *International Journal of Heat and Fluid Flow*, **23**-5, pp.639-646

Kajishima, T., 2004, "Influence of particle rotation on the interaction between particle clusters and particle-induced turbulence", *International Journal of Heat and Fluid Flow*, **25**-5, pp.721-728

Kang, S., Iaccarino, G., and Ham, F., 2009, "DNS of buoyancy-dominated turbulent flows on a bluff body using the immersed boundary method", *Journal of Computational Physics*, **228**, pp.3189-3208

Kim, J. and Choi, H., 2004, "An immersed-boundary finite-volume method for simulation of heat transfer in complex geometries", *KSME International Journal* **18** No.6, pp.1026-1035

Kim, J., Kim, D. and Choi, H., 2001, "An immersed-boundary finite-volume method for simulations of flow in complex geometries", *Journal of Computational Physics* **171**, pp.132-150

Kim, B.S., Lee, D.S., Ha, M.Y. and Yoon, H.S., 2008, "A numerical study of natural convection in a square enclosure with a circular cylinder at different vertical locations", *International Journal of Heat and Mass Transfer* **51**, pp.1888-1906

Lee, Y.O., Ahn, J. and Lee, J.S., 2007, "Effect of dimple arrangements on the turbulent heat transfer in a dimpled channel", *Proceedings of the 8th International Symposium on Transport Phenomena*, pp.480-485, Daejeon, Korea

McKenna, T.F., DuPuy, J. and Spitz, R., 1995, "Modeling of transfer phenomena on heterogeneous Ziegler catalysts: Differences between theory and experiment in olefin polymerization (an introduction)", *Journal of Applied Polymer Science* **57**, Issue 3, pp.371-384

McKenna, T.F., Spitz, R. and Cokljat, D., 1999, "Heat transfer from catalysts with computational fluid dynamics", *Reactors, Kinetics, and Catalysis* **45**, No.11, pp.2392-2410

Mittal, R., Iaccarino, G., 2005, "Immersed boundary methods", *Annual Review of Fluid Mechanics* **37**, pp.239-261

Moukalled, F., and Darwish, M., 1997, "New bounded skew central difference scheme, Part II: Application to natural convection in an eccentric annulus", *Numerical Heat Transfer Part B* **31**, pp.111-133

Nijemeisland, M. and Dixon, A.G., 2004, "CFD study of fluid flow and wall heat transfer in a fixed bed of spheres", *AIChE* **50** No.5, pp.906-921

Nishiura, D., Shimosaka, A., Shirakawa, Y. and Hidaka, J., 2006, "Hybrid simulation of hindered settling behavior of particles using discrete element method and direct numerical simulation" (in Japanese), *Kagaku Kogaku Ronbunshu*, **32**-4, pp.331-340

Pacheco, J.R., Pacheco-Vega, A., Rodić, T. and Peck, R.E., 2005, "Numerical simulations of heat transfer and fluid flow problems using an immersed-boundary finite-volume method on nonstaggered grids", *Numerical Heat transfer Part B*, **48**, pp.1-24

Pacheco-Vega, A., Pacheco, J. R. and Rodić, T., 2007, "A general scheme for the boundary conditions in convective and diffusive heat transfer with immersed boundary methods", *Journal of Heat Transfer*, **129**, Issue 11, pp.1506-1516

Pan, D., 2006, "An immersed boundary method on unstructured Cartesian meshes for incompressible flows with heat transfer", *Numerical Heat Transfer Part B* **49**, pp.277-297

Ren, W.W., Shu, C., Wu, J. and Yang, W.M., 2012, "Boundary condition-enforced immersed boundary method for thermal flow problems with Dirichlet temperature condition and its applications", *Computers & Fluids* **57**, pp.40-51

Takeuchi, S., Yuki, Y., Ueyama, A. and Kajishima, T., 2010, "A conservative momentum exchange algorithm for interaction problem between fluid and deformable particles", *International Journal for Numerical Methods in Fluids* **64**, Issue 10-12, pp.1084-1101

Tsuji,Y., Kawaguchi,T. and Tanaka,T., 1993, Discrete particle simulation of two-dimensional fluidized bed, *Powder Technology*, **77**, pp.79-87

Ueyama, A., Moriya, S., Nakamura, M. and Kajishima, T., 2011, "Immersed boundary method for liquid-solid two-phase flow with heat transfer", *Transaction of JSME Series B*, **77**-775, pp.803-814

Yoon, H.S., Lee, J.B. and Chun, H.H., 2007, "A numerical study on the fluid flow and heat transfer around a circular cylinder near a moving wall", *International Journal of Heat and Mass Transfer* **50**, pp.3507-3520

Yu, Z., Shao, X. and Wachs, A., 2006, "A fictitious domain method for particulate flows with heat transfer", *Journal of Computational Physics* **217**, pp.424-452

Yuki, Y., Takeuchi, S. and Kajishima, T., 2007, "Efficient immersed boundary method for strong interaction problem of arbitrary shape object with the self-induced flow", *Journal of Fluid Science and Technology*, **2**-1, pp.1-11

Zhang, N., Zheng, Z.C. and Eckels, S., 2008, "Study of heat-transfer on the surface of a circular cylinder in flows using an immersed-boundary method", *International Journal of Heat and Fluid Flow* **29**, pp.1558-1566

Acknowledgements

The authors gratefully acknowledge the financial supports of Grant-in-Aid for Scientific Research (B) No.23360085 and Grant-in-Aid for Young Scientist (A) No.23686030.

DOI: 10.1016/j.ijheatfluidflow.2013.05.013

Appendix A Construction of temperature field

We assume a solid-liquid two phase system, and a local volume fraction of fluid α_f is complemented with the solid volume fraction α; $\alpha_f = 1 - \alpha$.

Cell averaged heat capacity is given as $\overline{\rho c} = \alpha_f \rho_f c_f + \alpha_s \rho_s c_s$. The cell temperature $\widehat{T}$ is given by

$$\overline{\rho c}\,\widehat{T} = \rho_f c_f \langle X_f T_f \rangle + \rho_s c_s \langle X_s T_s \rangle \ ,$$

where $X_k\,(k = f, s)$ is indicator function, and $\langle X_k T_k \rangle$ is a phase-averaged temperature within a cell V_c given by $\frac{1}{V_c}\int_{V_c} X_k T_k\, dV = \frac{1}{V_c}\int_{X_k V_c} T_k\, dV \equiv \alpha_k \overline{T}_k$. With the cell-averaged temperature $\overline{T} = \langle X_f T_f + X_s T_s \rangle = (1 - \alpha)\overline{T}_f + \alpha \overline{T}_s$, $\widehat{T}$ is shown to follow:

$$\begin{aligned} \overline{\rho c}\,\widehat{T} &= \rho_f c_f (1-\alpha)\overline{T}_f + \rho_s c_s \alpha \overline{T}_s \\ &= \overline{\rho c}\,\overline{T} + \alpha(1-\alpha)(\rho_f c_f - \rho_s c_s)(\overline{T}_f - \overline{T}_s)\ . \end{aligned} \tag{10}$$

In the present study, we assumed the same heat capacity for the fluid and solid phases, therefore $\overline{T} = \widehat{T}$ follows.

Generally, the second term of the RHS of Eq.(10) is not zero. However, this is a second-order term with respect to the local volume fraction. Also, when the reference temperatures of fluid and solid in the cell are close enough (i.e.,$\overline{T}_f \simeq \overline{T}_s$), the term would be negligible, and the discrete temperature field $\overline{T}$ can be approximated by $\widehat{T}$.

Appendix B Decomposition of heat flux at the fluid-solid surface

Thermal diffusion term and heat flux

Let $X_k\,(k = f, s)$ is an indicator function for k-phase. Then, the interface is represented by $\nabla X_k\,(\stackrel{def}{=} -\widehat{\boldsymbol{n}}_k)$.

In the following, f and s stand for fluid and solid, respectively, and we allow a temperature gap at the surface ($T_{fI} \neq T_{sI}$), unless specified otherwise.

With the heat flux within k-phase ($\boldsymbol{q}_k = -\lambda_k \nabla T_k$), the thermal diffusion term at the interface cell is represented as follows:

$$\begin{aligned} -X_f \nabla\cdot(\lambda_f \nabla T_f) - X_s \nabla\cdot(\lambda_s \nabla T_s) &= X_f \nabla\cdot\boldsymbol{q}_f + X_s \nabla\cdot\boldsymbol{q}_s \\ &= \nabla\cdot\left[X_f \boldsymbol{q}_f + X_s \boldsymbol{q}_s\right] + \widehat{\boldsymbol{n}}_f\cdot\boldsymbol{q}_f + \widehat{\boldsymbol{n}}_s\cdot\boldsymbol{q}_s\ . \end{aligned} \tag{11}$$

Due to the conservation of the heat flux across the interface, the last two terms ($\widehat{\boldsymbol{n}}_f\cdot\boldsymbol{q}_f + \widehat{\boldsymbol{n}}_s\cdot\boldsymbol{q}_s$) vanish.

In the following, we only consider the terms within the divergence operator in Eq.(11). For a convenience, the flux is decomposed into the surface normal and tangential directions:

$$\begin{aligned} X_f \boldsymbol{q}_f + X_s \boldsymbol{q}_s &= -X_f \lambda_f \nabla T_f - X_s \lambda_s \nabla T_s \\ &= -(X_f \lambda_f \nabla T_f + X_s \lambda_s \nabla T_s)\cdot(\boldsymbol{I} - \boldsymbol{nn}) \\ &\quad -(X_f \lambda_f \nabla T_f + X_s \lambda_s \nabla T_s)\cdot\boldsymbol{nn} \\ &\stackrel{def}{=} \boldsymbol{q}\cdot(\boldsymbol{I} - \boldsymbol{nn}) + \boldsymbol{q}\cdot\boldsymbol{nn} \\ &\stackrel{def}{=} \boldsymbol{q}_t + \boldsymbol{q}_n\ . \end{aligned} \tag{12}$$

As we have determined to employ an Eulerian description for temperature, we try to represent the above flux, Eq.(12), with a single temperature field, $T \stackrel{def}{=} X_f T_f + X_s T_s$.

Surface tangential direction

Using the following identity equation,

$$\begin{aligned} & (X_f \lambda_f + X_s \lambda_s)(X_f \nabla T_f + X_s \nabla T_s) \\ = \ & X_f^2 \lambda_f \nabla T_f + X_s^2 \lambda_s \nabla T_s + X_f X_s (\lambda_f \nabla T_f + \lambda_s \nabla T_s) \\ & -X_f X_s (\lambda_f - \lambda_s)(\nabla T_f - \nabla T_s) \\ = \ & X_f \lambda_f \nabla T_f + X_s \lambda_s \nabla T_s - X_f X_s (\lambda_f - \lambda_s)(\nabla T_f - \nabla T_s)\ , \end{aligned} \tag{13}$$

the tangential component of the heat flux is given as follows:

$$\boldsymbol{q}_t \;=\; -(\lambda_a \nabla T)\cdot(\boldsymbol{I}-\boldsymbol{nn}) - X_f X_s(\lambda_f-\lambda_s)(\nabla T_f - \nabla T_s)\cdot(\boldsymbol{I}-\boldsymbol{nn}) \quad (\,\cdot_{\cdot}\cdot\ \widehat{\boldsymbol{n}}_s \perp (\boldsymbol{I}-\boldsymbol{nn}))\,, \tag{14}$$

where $\lambda_a \stackrel{def}{=} X_f\lambda_f + X_s\lambda_s$.

Surface normal direction

The distribution of the heat conductivities is given by the following function:

$$\lambda(\boldsymbol{x}) \text{ in } X_k \text{ region} : X_k\lambda_h\,, \quad \text{where} \quad \lambda_h \stackrel{def}{=} \frac{\lambda_f\lambda_s}{X_f\lambda_s + X_s\lambda_f}\,,$$

assuming that the indicator functions (X_f, X_s) is the algebraic functions complementarily taking the values 0 and 1.

$$\begin{aligned}
& (X_f\lambda_h)\nabla T_f + (X_s\lambda_h)\nabla T_s \\
=\;& (X_f\lambda_h + X_s\lambda_h)(X_f\nabla T_f + X_s\nabla T_s) \qquad (\,\cdot_{\cdot}\cdot \text{ from Eq.(13)}) \\
=\;& \lambda_h\left(\nabla(X_fT_f) + T_f\widehat{\boldsymbol{n}}_f + \nabla(X_sT_s) + T_s\widehat{\boldsymbol{n}}_s\right) \\
=\;& \lambda_h\nabla T + \lambda_h(T_s-T_f)\widehat{\boldsymbol{n}}_s. \\
\therefore\quad \boldsymbol{q}_n \;=\;& -(\lambda_h\nabla T)\cdot\boldsymbol{nn} - \lambda_h(T_s-T_f)\widehat{\boldsymbol{n}}_s\cdot\boldsymbol{nn}.
\end{aligned} \tag{15}$$

Assembly of both directions

Substituting Eqs.(15) and (14) into Eq.(12), a general expression for the heat flux within an interfacial cell:

$$\begin{aligned}
X_f\boldsymbol{q}_f + X_s\boldsymbol{q}_s \;=\;& -(\lambda_h\nabla T)\cdot\boldsymbol{nn} - (\lambda_a\nabla T)\cdot(\boldsymbol{I}-\boldsymbol{nn}) && \text{(16a)}\\
& -\lambda_h(T_s-T_f)\widehat{\boldsymbol{n}}_s\cdot\boldsymbol{nn} && \text{(16b)}\\
& -X_fX_s(\lambda_f-\lambda_s)(\nabla T_f-\nabla T_s)\cdot(\boldsymbol{I}-\boldsymbol{nn})\,. && \text{(16c)}
\end{aligned}$$

Here, let us consider a further simplified case; the surface temperatures of the f- and s-phases are the same ($T_{fI} = T_{sI} = T_I$), as assumed in the main body of the present paper. Then, the terms (16b) and (16c) are zero, since

$$\text{Derivative of } T_I \text{ along the surface} = \nabla T_f\cdot(\boldsymbol{I}-\boldsymbol{nn}) = \nabla T_s\cdot(\boldsymbol{I}-\boldsymbol{nn})\,.$$

Therefore, by assuming the coincidence of the surface temperatures, Eq.(16a) is simplified as follows:

$$X_f\boldsymbol{q}_f + X_s\boldsymbol{q}_s \;=\; -(\lambda_h\nabla T)\cdot\boldsymbol{nn} - (\lambda_a\nabla T)\cdot(\boldsymbol{I}-\boldsymbol{nn})$$

and finally, the thermal diffusion term in Eq.(11) yields:

$$\therefore\quad -\nabla\cdot\left[(\lambda_h\nabla T)\cdot\boldsymbol{nn} + (\lambda_a\nabla T)\cdot(\boldsymbol{I}-\boldsymbol{nn})\right]\,. \tag{17}$$

In the numerical implementation, the cell temperature is used after averaging the term over the cell, and the above two heat conductivities are approximated as follows:

$$\begin{aligned}
\lambda_a &= X_f\lambda_f + X_s\lambda_s \approx (1-\alpha)\lambda_f + \alpha\lambda_s \\
\frac{1}{\lambda_h} &= \frac{X_f}{\lambda_f} + \frac{X_s}{\lambda_s} \approx \frac{1-\alpha}{\lambda_f} + \frac{\alpha}{\lambda_s}\,,
\end{aligned}$$

where λ_h and λ_a are considered to be the effective heat conductivities in the normal and tangential directions, respectively.

DOI: 10.1016/j.ijheatfluidflow.2013.05.013

Appendix C Heat Conduction through Eccentric Cylinders

Double eccentric cylinders

Heat conduction through two eccentric cylinders is considered. A schematic for a heat conduction problem within double eccentric cylinders is illustrated in Fig.1(a). The corresponding problem on the ξ-η plane is depicted in Fig.1(b). Temperature is governed by the following equation:

$$\frac{\partial^2 T}{\partial \xi^2} + \frac{\partial^2 T}{\partial \eta^2} = 0 \, . \tag{18}$$

For the continuity of temperature and heat flux, we impose the following boundary conditions at $\xi = \xi_1$:

$$T_1(\xi_1, \eta) = T_2(\xi_1, \eta) \equiv T_m(\eta) \, , \tag{19}$$

$$\lambda_1 \left. \frac{\partial T_1}{\partial \xi} \right|_{\xi=\xi_1} = \lambda_2 \left. \frac{\partial T_2}{\partial \xi} \right|_{\xi=\xi_1} \, . \tag{20}$$

Through separation of the variables (ξ and η) for $T_1(\xi_1, \eta)$ together with the boundary condition Eq.(19) and $T_1(\xi_0, {}^\forall\eta) = 0$, the solution in region 1 is obtained as follows:

$$T_1(\xi, \eta) = \frac{2}{\pi} \sum_{n=1}^{\infty} \frac{\int_0^\pi T_m(\eta') \sin n\eta' \, d\eta'}{\sinh(n(\xi_0 - \xi_1))} \sinh(n(\xi_0 - \xi)) \sin n\eta \, . \tag{21}$$

The solution in region 2 is obtained in the same manner with the boundary condition $T_2(\xi_2, {}^\forall\eta) = T_h$ as follows:

$$\begin{aligned} T_2(\xi, \eta) \;\; = \;\; & \frac{2}{\pi} \sum_{n=1}^{\infty} \frac{\int_0^\pi T_m(\eta') \sin n\eta' \, d\eta' - \left\{ \begin{array}{cc} (2T_h/n)\cosh(n(\xi_1 - \xi_2)) & (n\text{:odd}) \\ 0 & (n\text{:even}) \end{array} \right\}}{\sinh(n(\xi_1 - \xi_2))} \sinh(n(\xi - \xi_2)) \sin n\eta \\ & + \frac{2}{\pi} \sum_{n=1,3,5,\cdots}^{\infty} \frac{2T_h}{n} \cosh(n(\xi - \xi_2)) \sin n\eta \, . \end{aligned} \tag{22}$$

Those two solutions, Eqs.(21) and (22), are obtained independently and include an unknown temperature distribution along the interface $T_m(\eta)$. Eq.(20) is imposed for determining T_m, and the Fourier sine coefficient of T_m is obtained as follows:

$$\int_0^\pi T_m(\eta') \sin k\eta' \, d\eta' = \left\{ \begin{array}{ll} \frac{2}{k} \left(\frac{\lambda_2}{\lambda_1 + \lambda_2} T_h \right) \frac{1}{\cosh(k\Delta\xi)} & (k : \text{odd number}) \\ 0 & (k : \text{even number}) \, . \end{array} \right.$$

where $\xi_0 - \xi_1 = \xi_1 - \xi_2 = \frac{\xi_0 - \xi_2}{2} \equiv \Delta\xi$ (i.e., $\xi_1 = \frac{\xi_0 + \xi_2}{2}$). Substituting the above equation into Eqs.(21) and (22), T_1 and T_2 are finally summarised into Eq.(7).

Heat conduction through M-layered eccentric cylinders

A schematic is shown in Fig.11. General solution of Eq.(18) in Region j is given as follows:

$$T_j = \sum_{n=1}^{\infty} \left(A_j^n \sinh(n(\xi - \xi_j)) + B_j^n \cosh(n(\xi - \xi_j)) \right) \sin n\eta \quad (M \geq j \geq 1) \, . \tag{23}$$

Hereafter, the boundary temperature at the left-hand end in each region (e.g., $\xi = \xi_j$ for region-j) is denoted as $\widetilde{T}_j(\eta)$. Multiplying $\sin k\eta$ to $T_j(\xi = \xi_j, \eta) = \widetilde{T}_j(\eta)$ and integrating it in the region of $0 \leq \eta \leq \pi$,

$$\sum_{n=1}^{\infty} B_j^n \int_0^\pi \sin n\eta \sin k\eta \, d\eta = \int_0^\pi \widetilde{T}_j(\eta') \sin k\eta' \, d\eta' \quad \rightarrow \; B_j^k = \frac{2}{\pi} \int_0^\pi \widetilde{T}_j(\eta') \sin k\eta' \, d\eta' \quad \left(\widetilde{T}_M = T_h \right) \, .$$

From $T_j(\xi=\xi_{j-1},\eta)=\widetilde{T}_{j-1}(\eta)$ together with the above B_j^k,

$$\begin{aligned} A_j^k &= \frac{1}{\sinh(k\Delta\xi)}\left[\frac{2}{\pi}\int_0^\pi \widetilde{T}_{j-1}\sin k\eta'\,d\eta' - B_j^k\cosh(k\Delta\xi)\right] \\ &= \frac{2/\pi}{\sinh(k\Delta\xi)}\int_0^\pi \left[\widetilde{T}_{j-1}-\widetilde{T}_j\cosh(k\Delta\xi)\right]\sin k\eta'\,d\eta' \ , \end{aligned}$$

where $\Delta\xi=\xi_{j-1}-\xi_j\ (^\forall j)$. Therefore, the solution in region-j (Eq.(23)) is represented with the boundary temperatures, $\widetilde{T}_{j-1}$ and $\widetilde{T}_j$ as follows:

$$\begin{aligned} T_j &= \frac{2}{\pi}\sum_{n=1}^\infty\left[\int_0^\pi \frac{\widetilde{T}_{j-1}-\widetilde{T}_j\cosh(n\Delta\xi)}{\sinh(n\Delta\xi)}\sin n\eta'\,d\eta'\right]\sinh(n(\xi-\xi_j))\sin n\eta \\ &\quad +\frac{2}{\pi}\sum_{n=1}^\infty\left[\int_0^\pi \widetilde{T}_j\sin n\eta'\,d\eta'\right]\cosh(n(\xi-\xi_j))\sin n\eta \qquad (M\geq j\geq 1)\ . \end{aligned} \tag{24}$$

Substituting the above T_j into the continuity of heat flux (across the adjacent regions):

$$\lambda_j\left.\frac{\partial T_j}{\partial\xi}\right|_{\xi_{j-1}} = \lambda_{j-1}\left.\frac{\partial T_{j-1}}{\partial\xi}\right|_{\xi_{j-1}} \qquad (M\geq j\geq 2)\ ,$$

the following recurrence formula is obtained:

$$-\lambda_{j-1}\int_0^\pi \widetilde{T}_{j-2}\sin k\eta'\,d\eta' + (\lambda_{j-1}+\lambda_j)\cosh(k\Delta\xi)\int_0^\pi \widetilde{T}_{j-1}\sin k\eta'\,d\eta' - \lambda_j\int_0^\pi \widetilde{T}_j\sin k\eta'\,d\eta' = 0\ .$$
$(M\geq j\geq 2)$.

Here, the boundary values for the above recurrence formula are:

$$\int_0^\pi \widetilde{T}_0(\eta')\sin k\eta'\,d\eta' = 0 \tag{25}$$

$$\int_0^\pi \widetilde{T}_M(\eta')\sin k\eta'\,d\eta' = T_h\int_0^\pi \sin k\eta'\,d\eta' = \begin{cases} 2T_h/k & (k:\text{odd}) \\ 0 & (k:\text{even}) \end{cases}\ . \tag{26}$$

Solving the above recurrence formula, $\int_0^\pi \widetilde{T}_j\sin k\eta'\,d\eta'$ is substituted into Eq.(24) for $T_j(\xi,\eta)$.

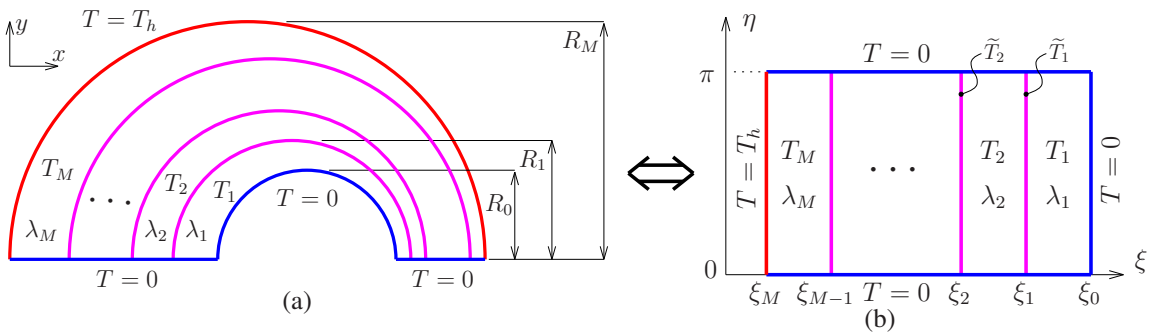

Figure 11: Schematic of a heat conduction problem through M-layered eccentric cylinders and the converted plane.